Predicting Adsorption Affinities of Small Molecules on Carbon Nanotubes Using Molecular Dynamics Simulation

Jeffrey Comer,[*,†,‡,§] **Ran Chen,**[†,‡] **Horacio Poblete,**[†,‡,§] **Ariela Vergara-Jaque,**[†,‡,§] **and Jim E. Riviere**[†,§]

[†]Institute of Computational Comparative Medicine, [‡]Nanotechnology Innovation Center of Kansas State, and [§]Department of Anatomy and Physiology, Kansas State University, Manhattan, Kansas 66506-5802, United States

ABSTRACT Computational techniques have the potential to accelerate the design and optimization of nanomaterials for applications such as drug delivery and contaminant removal; however, the success of such techniques requires reliable models of nanomaterial surfaces as well as accurate descriptions of their interactions with relevant solutes. In the present
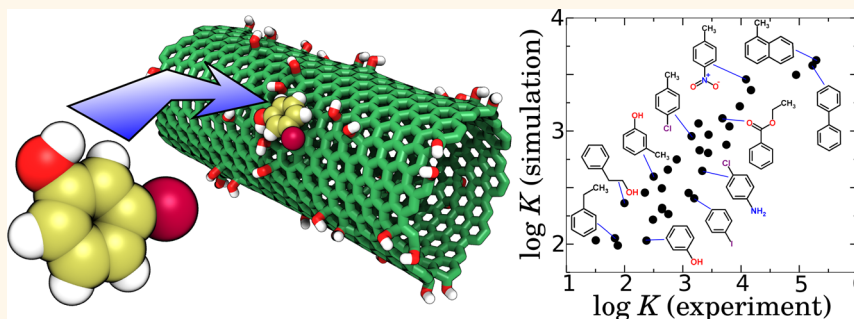
work, we evaluate the ability of selected models of naked and hydroxylated carbon nanotubes to predict adsorption equilibrium constants for about 30 small aromatic compounds with a variety of functional groups. The equilibrium constants determined using molecular dynamics coupled with free-energy calculation techniques are directly compared to those derived from experimental measurements. The calculations are highly predictive of the relative adsorption affinities of the compounds, with excellent correlation ($r \geq 0.9$) between calculated and measured values of the logarithm of the adsorption equilibrium constant. Moreover, the agreement in absolute terms is also reasonable, with average errors of less than one decade. We also explore possible effects of surface loading, although we demonstrate that they are negligible for the experimental conditions considered. Given the degree of reliability demonstrated, we move on to employing the *in silico* techniques in the design of nanomaterials, using the optimization of adsorption affinity for the herbicide atrazine as an example. Our simulations suggest that, compared to other modifications of graphenic carbon, polyvinylpyrrolidone conjugation gives the highest affinity for atrazine—substantially greater than that of graphenic carbon alone—and may be useful as a nanomaterial for delivery or sequestration of atrazine.

KEYWORDS: nanoparticles · free-energy calculations · surface physicochemistry · virtual screening · benzene derivatives · graphene · surface functionalization · aromatic

Given their large surface-area-to-volume ratios, the physical chemistry of nanomaterials is dominated by their surface interactions and, in particular, their ability to adsorb smaller molecules onto their surfaces. In nanomedicine, these interactions permit nanomaterials to deliver high loads of drugs and target specific cells or tissues.[1−3] Moreover, nanomaterials *in vivo* typically possess a "corona" of adsorbed proteins on their surfaces[4−6] that affects their cellular uptake,[7,8] physiological distribution and excretion,[7,9,10] and interaction with the immune[11−13] and coagulation systems.[14,15] Outside of living organisms, surface interactions drive applications of nanomaterials in purification of biological molecules[16−18] and removal of contaminants[19−23]

from complex mixtures. With particular relevance for the materials considered in the present work, carbon nanotubes are used as superior substrates in solid phase extraction,[24] allowing sensitive detection of environmental contaminants[25,26] including agricultural chemicals such as the widely used herbicide atrazine.[27,28]

However, designing nanomaterials to obtain desired surface interactions remains a challenge. Nanomaterials today are based on a wide range of carbon allotropes, metals, ceramics, and synthetic polymers, which may be surface-modified with a wide variety of functional groups. Such enormous diversity promises to drive revolutions in many fields; however, little guidance exists in sorting through the astronomical number

of possibilities to find optimal solutions. In the field of drug design, computational methods have been applied to solve similar problems,[29−33] permitting the rapid screening of candidate compounds for high affinity to the target and, importantly, insight into the atomic-level interactions giving rise to this affinity. The application of such approaches to nanomaterial design is fairly new.[34] Recent work has been directed at computational tools for predicting the toxicity of nanomaterials,[35] their cellular uptake,[36] and their biological activity.[37]

To assess surface interactions specifically, coauthors of the present work have developed a surface adsorption index,[38−40] wherein the adsorption properties of adsorbates are assumed to be governed by selected molecular descriptors (e.g., molecular volume, polarizability, hydrogen-bond acidity or basicity). A structure−activity relationship linking these descriptors to the adsorption equilibrium constant is found for each nanomaterial of interest, parametrized by measuring this equilibrium constant for a training set of small molecules. It was demonstrated that this surface adsorption index can reliably predict adsorption affinities for distinct sets of adsorbates on a wide range of nanomaterials, including naked and functionalized carbon nanotubes. However, a limitation is that experiments must be performed to characterize each new nanomaterial surface. For nanomaterial design and screening, it would be useful if the surface adsorption index could be determined *in silico*, directly from the physicochemical properties of the nanomaterial. Here, we explore whether computational techniques can be used to rapidly estimate adsorption constants of organic molecules on nanomaterials while also revealing nanoscale interactions that drive adsorption.

In recent years, molecular dynamics simulation with atomistic models and explicit solvent has been applied to elucidate interactions between common nanomaterials and organic molecules. For example, simulation has provided insight on peptide adsorption[41] on metals[42−44] and carbon nanotubes.[45] The encapsulation of drugs and nucleic acids by dendrimers[46−50] and polymer-based nanoparticles[51,52] has also been better understood through simulation. Brancolini et al.[53] studied binding of a complete protein to naked and citrate-coated gold surfaces using docking and molecular simulation, while Carr et al.[54] considered protein adsorption to an amorphous silica surface under hydrodynamic flow. Moreover, free-energy calculation techniques, based on biased sampling, permit molecular dynamics simulation to explore the thermodynamics of long time scale processes.[33,55−59] With sufficiently accurate interatomic potentials for the materials of interest, these techniques are capable of yielding precise agreement with experiment for free energies of binding.[60−63] For nanomaterials, free-energy techniques have been used to calculate adsorption affinities of amino acids on model

gold,[64−67] silver,[68] zinc oxide[69] surfaces, and graphenic materials,[70,71] as well as for contaminants on amorphous silica.[72] For carbon nanotubes, Klein and co-workers computed adsorption free energies of DNA, revealing the base selectivity and most thermodynamically favorable conformations of DNA-wrapped carbon nanotubes,[73,74] while Lin et al.[75] performed similar calculations for adsorption of several surfactants. Especially relevant to the present work is a study by Ulissi et al.[76] in which free energies of adsorption on a graphenic surface were computed for more than 50 compounds and exhibited good correlation with the predictions of structure−activity models.

Reliable predictions from molecular models of nanomaterials require both a realistic representation of the nanomaterial structure and an accurate description of the forces between atoms of the adsorbate, nanomaterial, and solvent (i.e., an accurate force field). For some materials, such as unmodified carbon nanotubes with few defects, the structure of the surface is well known. However, for other materials, the surface chemistry and topography at the atomic scale is not well known, and these may be sensitive to details of the synthesis and may vary considerably among different nanoparticles or at different locations on the same nanoparticle. For example, the density of hydroxyl groups on the surface of hydroxylated carbon nanotubes can depend on the oxidant used to create these groups.[77]

In the present work, we leverage experimental measurements of small-molecule adsorption[39,40] to test whether a number of plausible models of carbon nanotubes combined with a classical molecular dynamics force field can predict adsorption properties in agreement with the experiments. Free-energy calculations are performed with all-atom explicit-solvent models to determine the potential of mean force of each aromatic adsorbate as a function of distance from the model surfaces. On the basis of a theoretical derivation, we compute adsorption equilibrium constants from these potentials, which should be directly comparable to experimental values. The adsorption equilibrium constants determined from the simulation are of similar orders of magnitude to the values derived from experiment and show a high degree of correlation with the latter values, implying that the simulations reliably predict the relative affinities of the different aromatic compounds. We also consider several possible models of hydroxylated nanotube surfaces and find the best agreement with experiment for one of the most plausible. With this validation of the molecular dynamics approach to estimating adsorption affinity, we perform similar free-energy calculations for polymer-conjugated carbon nanotubes with an aromatic herbacide widely used in agriculture for weed control[78] serving as the adsorbate.

RESULTS AND DISCUSSION

Theoretical Link between Experiment and Simulation. In the relevant experiments,[39,40] a solution containing various concentrations of several small aromatic compounds is added to a vial containing a colloid of water and a known mass of nanoparticles (nanotubes). The final concentration of compound not adsorbed to the nanoparticles is accurately measured using solid phase microextraction and gas chromatography mass spectrometry. Thus, the adsorption affinity for a given compound, i, is conveniently characterized by an adsorption equilibrium constant

$$K_i^{expt} = \frac{V(c_i^0 - c_i^{eq})}{mc_i^{eq}} = \frac{V}{m}\frac{N_{i:NP}^{eq}}{N_i^{eq}} \qquad (1)$$

where V is the volume of liquid in the vial, c_i^0 is the concentration of compound i in the vial prior to contact with the nanoparticles, c_i^{eq} is the concentration of free compound i remaining in the vial after equilibrium has been reached, and m is the total mass of nanoparticles. $N_{i:NP}^{eq}$ and N_i^{eq} are the equilibrium numbers of compound i adsorbed to the nanoparticle and remaining free in solution, respectively.

For the lowest concentration considered in the experiments, the surface density of adsorbed molecules is relatively low. By eq 1, we can find the surface density of each compound by $S_i = (M_{NP}/A_{NP})(V/m)(c_i^0 - c_i^{eq})/M_i$, where M_i is the molecular mass of component i and A_{NP}/M_{NP} is the specific surface area of the nanotubes. Summing over all compounds, we obtain a total surface density of $\sum_i S_i = 0.013$ molecules/nm^2, which implies a typical distance of about 8.8 nm between each molecule, much larger than the diameter of the molecules (the largest, biphenyl, has a diameter of $\sim$1.0 nm). Thus, for much of the present work, we neglect interactions among adsorbates, although we consider such interactions in the section Adsorption under Conditions of Significant Surface Loading.

The ratio $N_{i:NP}^{eq}/N_i^{eq}$ in eq 1 can be estimated from free-energy calculations, given by[72]

$$\frac{N_{i:NP}^{eq}}{N_i^{eq}} = \frac{\int_{ads} d\mathbf{r}\,\exp[-\beta w_i(\mathbf{r})]}{\int_{free} d\mathbf{r}\,\exp[-\beta w_i(\mathbf{r})]} \qquad (2)$$

where the integrals in the numerator and denominator are over molecule positions in the adsorbed and free regions of space, $\beta = (k_B T)^{-1}$ is the reciprocal thermal energy, and $w_i(\mathbf{r})$ is the potential of mean force[59] as a function of the three-dimensional position in the vial. By convention, $w(\mathbf{r}) = 0$ for positions of the molecule $\mathbf{r}$ far from any nanoparticle. Assuming that the colloid is sufficiently dilute, we can approximate the denominator of eq 2 by V. Because the typical diameters of the nanomaterials considered in this work ($\geq$8 nm) are much larger than those of the small aromatic

compounds ($<$1 nm), we assume that the overall curvature of the cylindrical nanotubes has a negligible effect on adsorption of the compounds.[76] Thus, in the simulation, each nanomaterial is represented by a patch of solid surface, with an interface roughly corresponding to the xy plane. We perform free-energy calculations[59] to obtain $w_i^{calc}(z)$, the potential of mean force as a function of the distance between the center of mass of compound i and a reference plane at the nanoparticle interface. Given sufficient sampling, $w_i^{calc}(z)$ incorporates any lateral variability in the adsorption affinity. This has been verified for the calculations here in Figures S2−4 in the Supporting Information (SI). Equation 2 can therefore be written

$$\frac{N_{i:NP}^{eq}}{N_i^{eq}} \approx \frac{N_{NP}A_{NP}}{V}\int_0^c dz\,\exp[-\beta w_i^{calc}(z)] \qquad (3)$$

where N_{NP} is the number of nanoparticles in the vial, A_{NP} is the typical accessible surface area of a single nanoparticle, and c is a distance cutoff defining the adsorbed region. For the systems considered here, all reasonable definitions of the integration limit c yield effectively identical K_i values, as verified in Figure S9 of the SI. Substituting eq 3 into eq 1 gives us a route to estimate the adsorption equilibrium constant from the simulations:

$$K_i^{calc} = \frac{A_{NP}}{M_{NP}}\int_0^c dz\,\exp[-\beta w_i^{calc}(z)] \qquad (4)$$

where $M_{NP} = m/N_{NP}$ is the typical mass of a single nanoparticle. The specific surface area $A_{NP}/M_{NP} = 233$ m^2/g is experimentally determined by the Brunauer−Emmett−Teller method.[39] Further discussion of the appropriateness of eq 4 for the nanotubes used in the experiment can be found in the SI.

Adsorption on Multiwall Carbon Nanotubes. We now consider adsorption onto large carbon nanotubes, which is a particularly simple case given that the chemical structure and topography of the surface are well known and homogeneous (barring large densities of defects). The carbon nanotubes used in the experiments to which we are comparing were characterized by transmission electron microscopy as having outer diameters of 8−15 nm and lengths of $\sim$50 μm. The number of walls within these multiwall nanotubes and the spacing between them are unknown (see the section Considerations of the Appropriateness of the Theory in the SI for an analysis). We postulate that a few flat graphene sheets should represent the typical local environment of the adsorbate. Figure 1A shows an example of the models used in the molecular dynamics simulations. The presence of four graphene sheets *versus* a single graphene sheet has only a mild effect on K_i^{calc} (see Figure S8 of the SI), implying that such models are reasonable representations of any relatively flat graphenic surface, including free-standing graphene and graphene nanoplatelets. We note that
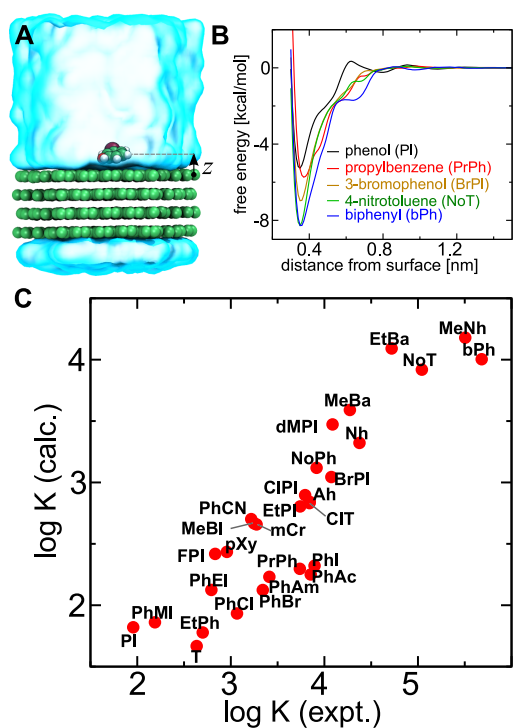
Figure 1. Comparison of experiment and simulation for adsorption on naked carbon nanotubes. (A) Model for molecular dynamics simulation of adsorption of small molecules onto the surface of multiwall carbon nanotubes. The relatively large multiwall nanotubes are modeled as several flat graphene sheets, which, through periodic boundary conditions, form an effectively infinite surface in the xy plane. The atoms of the graphene sheets and an exemplary adsorbate (3-bromophenol) are shown as spheres, with hydrogen, carbon, oxygen, and bromine atoms shown in white, green, red, and crimson, respectively. Here, for clarity, the water is indicated by a translucent cyan surface; however, in the simulations, water molecules were represented explicitly. (B) Calculated free energy as a function of distance between the first graphene sheet and the center of mass of the adsorbate (the coordinate z) for exemplary adsorbates. (C) Comparison of the logarithm of the adsorption equilibrium constant measured in experiment and the same quantity calculated in simulation for all 29 adsorbates. Following Chen et al.,[40] the adsorption constant K (in units of mL/g) is defined according to eq 1. Values derived from simulation are calculated using eq 4 and the free-energy profiles, such as those shown in panel B. The abbreviations of the compounds used here are listed in Table 1.

our models and approach to computing adsorption free energies on nanotubes are similar to those of Ulissi et al.[76] As in previous work,[79] we model graphene by a simple adaptation of the CHARMM additive force field,[80] while the parameters describing the small aromatic molecules were obtained from the CHARMM general force field (CGenFF). While force fields explicitly accounting for electronic polarizability[81,82] have the potential to improve accuracy of molecular dynamics simulation and can be applied to a growing range of molecules,[83−86] force fields with fixed atomic charges have the advantage of decades of refinement, lower computational cost, and calibrated parameters for a wider variety for materials. Recent work has used a polarizable model to study adsorption at graphenic

TABLE 1. List of Adsorbate Molecules Considered in This Work[a]

abbrev	compound name	substituent	halogen
Ah	acetophenone	ketone	
bPh	biphenyl	aromatic	
BrPl	3-bromophenol	hydroxyl	X
ClAh	4-chloroacetophenone	ketone	X
ClAn	4-chloroanisole	ether	X
ClPl	3-chlorophenol	hydroxyl	X
ClT	4-chlorotoluene	alkyl	X
dMPl	3,5-dimethylphenol	alkyl, hydroxyl	
EtBa	ethylbenzoate	ester—alkyl	
EtPh	ethylbenzene	alkyl	
EtPl	4-ethylphenol	alkyl, hydroxyl	
FPl	4-fluorophenol	hydroxyl	X
mCr	*m*-cresol	alkyl, hydroxyl	
MeBa	methylbenzoate	ester—alkyl	
MeBl	(3-methylphenyl)methanol	alkyl, hydroxyl	
MeNh	1-methylnaphthalene	aromatic	
MMBa	methyl-2-methyl benzoate	alkyl, ester—alkyl	
Nh	naphthalene	aromatic	
NoPh	nitrobenzene	nitro	
NoT	4-nitrotoluene	alkyl, nitro	
PhAc	phenylacetate	ester—alkyl	
PhAm	4-chlorophenylamine	amine	X
PhBr	bromobenzene		X
PhCl	chlorobenzene		X
PhCN	benzonitrile	nitrile	
PhEl	2-phenylethanol	alkyl—hydroxyl	
PhI	iodobenzene		X
PhMl	phenylmethanol	alkyl—hydroxyl	
Pl	phenol	hydroxyl	
PrPh	propylbenzene	alkyl	
pXy	*p*-xylene	alkyl	
T	toluene	alkyl	

[a] For clarity in our plots, the compounds are indicated by the short, but sometimes nonstandard abbreviations given here. The other columns indicate how the molecule differs from a benzene prototype and whether the compound is halogenated.

surfaces,[70,71] although the polarizability was represented only in graphene, while the adsorbates and water used fixed charge models. It is not yet completely clear that the increased computational expense of existing polarizable models (which translates into less simulated time and, thus, poorer sampling) is justified by greater accuracy.[85]

For unmodified multiwall carbon nanotubes, experimentally derived adsorption equilibrium constants[40] are available for 29 of the 32 small aromatic compounds detailed in Table 1. These molecules have a variety of functional groups, including some common biological motifs, while others may be relevant for understanding interactions with drug molecules, *e.g.*, the halogenated compounds. For each adsorbate, we performed a free-energy calculation using the adaptive biasing force[59,87,88] technique to determine the potential of mean force as a function of the distance between the center of mass of each adsorbate and the plane passing through the centers of the carbon atoms in the first layer of graphene, $w_i^{calc}(z)$. The convergence of $w_i^{calc}(z)$ during

the free-energy calculations was carefully monitored as summarized in Figure S1 of the SI.

Figure 1B shows the potentials of mean force for a few representative compounds. At large distances, $z > 1.4$ nm, the interaction between the surface and adsorbate becomes negligible, yielding a plateau at a fixed value, which by convention is anchored to zero. On the other hand, steric interaction leads to a rapidly rising free energy as the adsorbate attempts to penetrate the surface ($z < 0.33$ nm). Given the relatively hydrophobic natures of both the small aromatics and carbon nanotubes,[89] one would expect adsorption to be thermodynamically favored. Indeed, we find minima in the potentials of mean force with magnitudes of several times the thermal energy for all adsorbates, occurring at distances from $z = 0.35$ to 0.37 nm. The deepest free-energy well of -8.7 kcal/mol is seen for 1-methylnaphthalene, while the shallowest is for toluene. As exemplified in Figure 1A, in all cases the lowest free-energy configuration corresponds to the adsorbates lying flat on the graphene, with the aromatic moieties parallel to the surface.

The fraction of adsorbed molecules is not determined solely by the depth of the free-energy well, but also by its shape, according to eq 4. For example, although 4-nitrotoluene possesses a slightly deeper minimum in Figure 1B than biphenyl, the larger size of biphenyl leads to a broader well, which gives it a larger equilibrium constant. Because the potential of mean force appears in an exponent in eq 4, only the few points with free-energy values near the global minimum contribute significantly to the equilibrium constant; however, accurate determination of $w_i^{calc}(z)$ out to the plateau is required to characterize the free-energy difference between adsorbed and free states. Invoking mean first-passage time theory,[90] one can also calculate rates of desorption from the potentials of mean force and position-dependent diffusivity. The latter is obtained from simulation trajectories by a previously reported method.[91] As shown in Figure S10 of the SI, typical times for escaping the free-energy minimum to reach a distance of 1.5 nm range from ∼100 ns for phenol to ∼30 μs for biphenyl.

We plot $\log_{10} K_i^{calc}$ against the corresponding experimentally determined value for each compound in Figure 1C. Substantial linear correlation of $\log_{10} K_i^{expt}$ and $\log_{10} K_i^{calc}$ is unmistakable and can be quantified by a Pearson correlation coefficient of $r = 0.90$. Furthermore, in absolute terms, values of $\log_{10} K_i^{expt}$ range from 2.0 to 5.7, while those of $\log_{10} K_i^{calc}$ occupy a similar range of 1.7 to 4.2. Thus, there is excellent consistency between experiment and simulation in the relative values for different adsorbates and substantial agreement in an absolute sense as well, although some discrepancies are apparent, as will be discussed further below.

Figure 1C demonstrates that the simulations yield many insights that would be difficult to predict

from basic chemical principles. Although the surface of carbon nanotubes is considered to be relatively hydrophobic,[89] the hydrophobicity of an adsorbate, as characterized by its octanol−water partition coefficient, $\log_{10} P_i^{OW}$, is a poor predictor of $\log_{10} K_i^{expt}$ with a correlation coefficient of only $r = 0.53$. For example, with its polar nitro group, 4-nitrotoluene is only moderately hydrophobic, with $\log_{10} P_{NoT}^{OW} = 2.4$; however, both experiment and simulation assert that it adsorbs strongly to carbon nanotubes, much more strongly than, for instance, propylbenzene, for which $\log_{10} P_{PrPh}^{OW} = 3.7$. The enhanced adsorption of nitroaromatics with respect to other aromatics on carbon nanotubes has been recognized previously and attributed to strong $\pi-\pi$ interactions,[92,93] which are implicitly and approximately represented by the classical models used here.[94] Previous experimental work[92] also corroborates our observation that chlorination of the benzene ring increases adsorption, which can be clearly seen for toluene and 4-chlorotoluene in both experiment and simulation. No simple property appears to completely predict the affinity; indeed, the surface adsorption index (structure−activity model) developed by Riviere and co-workers[39,40] relates the adsorption equilibrium constant to a set of five molecular descriptors. The molecular dynamics approach compares well to this structure−activity model, which attained only slightly better correlation ($r = 0.92$) when applied to a set of molecules distinct from those used to parametrize it.[40] In terms of computational cost, free-energy calculations required a few days of continuous simulation on a modest computing cluster, while the surface adsorption index is effectively free. On the other hand, parametrizing the surface adsorption index required experimental assays to characterize each new nanomaterial. What is remarkable about the results of the simulations presented here is that they require only information on the chemical structures of the surface and adsorbate. Thus, Figure 1C shows that, at least in this case, one could parametrize the surface adsorption index with relatively high accuracy from computation alone, avoiding costly, labor-intensive experiments.

Despite the fact that the calculations may yield useful predictions of relative affinity, some discrepancies can be identified, most notably the fact that the adsorption affinity appears systematically underestimated, with $\log_{10} K_i^{calc}$ deviating from $\log_{10} K_i^{expt}$ by -0.92 on average. Another perceptible disagreement is that the spread of $\log_{10} K_i^{calc}$ is somewhat smaller than that of $\log_{10} K_i^{expt}$, as characterized by standard deviations of 0.73 and 0.89. Plotting a least-squares fit line through the data in Figure 1C, we find that all of the halogenated benzenes (PhCl, PhBr, PhI) and alkyl-substituted benzenes (T, EtPh, PrPh), except pXy, lie below the fit line, while the benzoates and nitro compounds are located above it. Therefore, it appears that, with respect to the experiments, the adsorption affinities of adsorbates
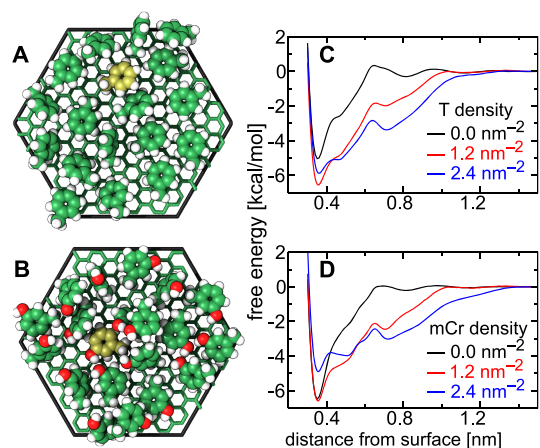
Figure 2. Adsorption on carbon nanotube surfaces with significant surface loading. (A, B) Toluene or *m*-cresol adsorption on surfaces loaded with like molecules. The carbons of the molecule that is the subject of the free-energy calculation are shown in yellow. The surface density of the remaining molecules is 2.4 nm^{-2}. (C, D) Calculated free-energy profiles for toluene/*m*-cresol adsorption on bare or toluene/*m*-cresol-loaded surfaces.

with nonpolar substituents are underestimated relative to those with polar moieties. Another possibility is inaccuracy in the specific surface area derived from the experiments in the context of small-molecule adsorption; however, different estimates of A_{NP}/M_{NP} will result only in a uniform shift of all $\log_{10} K_i^{calc}$ values, so the specific surface area has no bearing on the correlation coefficient nor the standard deviations quoted above.

Adsorption under Conditions of Significant Surface Loading. So far we have considered the dilute limit, neglecting interactions between adsorbed molecules. However, even when solutes are present only at low ambient concentrations, those with high adsorption affinity can occupy a non-negligible fraction of the surface. Indeed, such high loading of the surface is desirable for applications in drug delivery and decontamination. Heavy loading of small molecules on the surface to form a homogeneous adsorbed phase poses little difficulty for the approach applied above, assuming the time for rearrangement of the adsorbed molecules is much shorter than the simulated times. In Figure 2 we consider adsorption of an additional molecule to surfaces already loaded with the same molecules at multiple densities. Although adsorption remains chiefly in a monolayer, at the highest concentrations, Figure 2C,D show local minima near $z = 0.71$ nm, indicating the formation of a weakly bound second layer. Interestingly, we observe that adsorption becomes more favorable as the surface density of molecules is increased from 0 to 1.2 nm^{-2}, which is especially significant for toluene. While a loading of 1.2 nm^{-2} increases the adsorption affinity, higher levels appear to have the opposite effect. In both cases, doubling the surface density to 2.4 nm^{-2} results in decreased adsorption affinity likely due to steric effects. In the case of *m*-cresol, the adsorption

affinity at a loading of 2.4 nm^{-2} is less than even on a pristine surface. Thus, depending on the surface density, loading led to both significant increases and significant decreases in adsorption affinity.

Although the total surface density in the experiment was considerably lower ($\sim$0.013 nm^{-2}), it would be prudent to determine the magnitude of corrections due to loading. The low density of 32 different components used in experiment yields a heterogeneous adsorbed phase at the molecular scale, posing a significant challenge for sampling in explicit-solvent molecular dynamics. To describe heterogeneous adsorbed phases, Ulissi *et al.*[76] have combined results from molecular dynamics with an analytical model of multicomponent adsorption. As an alternative to the analytical approach, here we leverage results of explicit-solvent molecular dynamics to build a large-scale implicit-solvent simulation using Brownian dynamics with grand-canonical Monte Carlo.[95] The details of these simulations are given in the section Grand-Canonical Monte Carlo/Brownian Dynamics in the SI. As described there, we find that accounting for interactions between adsorbates has only a negligible effect on $\log_{10} K_i^{calc}$. Thus, intermolecular interactions are probably not sufficient to explain the discrepancies between simulation and experiment and are neglected for the rest of this paper.

Adsorption on Hydroxylated Multiwall Carbon Nanotubes. We now move to the case of hydroxylated nanotubes, which is more complex due to the lack of information on the spatial arrangement of OH groups on the nanotube surface. In the SI of the original reference,[39] the quantity of OH groups was given as 3.70% by weight. Thus, the number of OH groups per unit area can be estimated by $S_{OH} = (M_{NP}/A_{NP})M_{OH}f$, where $f = 0.037$ is the fraction of OH groups by weight and $M_{OH} = 17.01$ Da is the mass of an OH group. The density of OH on the surface of the nanotubes should be roughly 5.6 nm^{-2}. How to arrange these groups along the surface, however, is not altogether clear. The most obvious way, which may not be physically motivated, is to distribute them uniformly. On the other hand, hydrogen-bond interactions between OH groups may favor configurations where multiple groups are placed nearby.[96] Here we consider several densities and arrangements, rendered in Figure 3. Highly symmetric arrangements that tiled the system's periodic cell were chosen to accelerate conformational averaging in the free-energy calculations. As shown in Figures S2 and S3 in the SI, the arrangement of the OH groups strongly affects the conformational ensemble of adsorbed molecules. The models considered in Figure 3 may also be relevant for graphene oxide; however, a more realistic graphene oxide model might include epoxide groups in addition to hydroxyls.[96]

The comparison of $\log_{10} K_i^{expt}$ and $\log_{10} K_i^{calc}$ for the various hydroxylated graphene models is summarized in Table 2, with the results for the model of naked
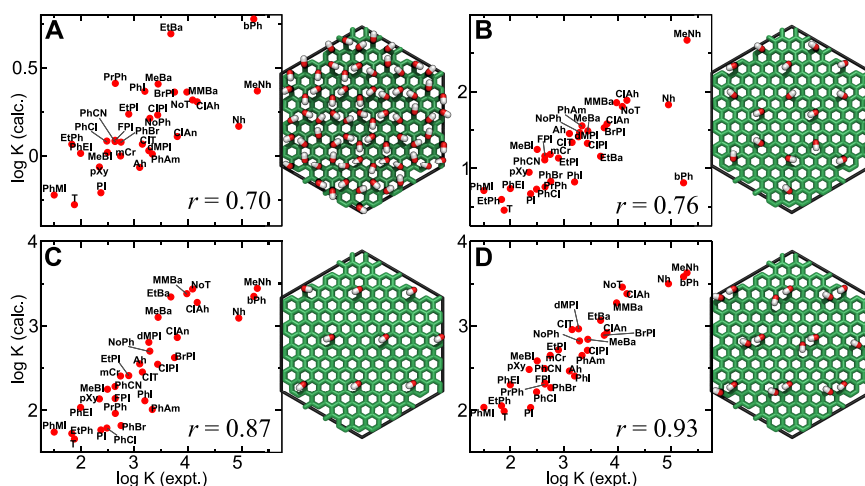
Figure 3. Comparison of experiment and simulation for different models of hydroxylated carbon nanotubes. The experimental $\log_{10} K$ values, plotted on the horizontal axis, are identical in each plot, while the $\log_{10} K$ values on the vertical axis are derived from simulations using the arrangement of OH groups illustrated to the right of the plot. The Pearson correlation coefficients (r) of the experimental and calculated values are indicated with the plots. Note that the vertical scales vary among the plots. The OH groups were free to rotate in the simulations; thus, only one exemplary configuration is shown. The systems used here are identical to that shown in Figure 1A except for the addition of the OH groups; only the uppermost graphene sheet is shown for clarity. The OH group arrangements were chosen to regularly tile the hexagonal periodic cell of the system.

TABLE 2. Summary of Comparison between Experimental and Calculated Adsorption Constants on Carbon Nanotubes for a Set of Small Aromatics[a]

expt syst	model	density OH [nm^{-2}]	no. of compounds	RMS error	mean deviation	correlation coeff
MWCNT	graph	0.0	29	0.99	−0.92	0.90
MWCNT−OH	graph−OH(A)	9.6	31	3.10	−3.00	0.70
MWCNT−OH	graph−OH(B)	2.4	31	2.05	−1.94	0.75
MWCNT−OH	graph−OH(C)	1.2	31	0.85	−0.68	0.87
MWCNT−OH	graph−OH(D)	2.4	31	0.69	−0.47	0.93

[a] "Expt syst" indicates the naked or hydroxylated multiwall carbon nanotubes used in the experiments of Xia et al.[39] and Chen et al.[40] The definitions of the "RMS error" and "mean deviation" are described in the text.

carbon nanotubes included for reference. The RMS error, calculated by

$$\left(\frac{1}{n} \sum_{i=1}^{n} [\log_{10} K_i^{calc} - \log_{10} K_i^{expt}]^2 \right)^{1/2} \quad (5)$$

indicates the typical absolute error for individual compounds, while the "mean deviation", defined by $\langle \log_{10} K_i^{calc} \rangle - \langle \log_{10} K_i^{expt} \rangle$, gives some sense of the systematic deviation between the experimental and calculated results. The fact that the mean deviation is in all cases negative shows that the simulations systematically underestimate the strength of adsorption with respect to the experiments. However, for some models this bias is quite large, while for others it is less considerable. Furthermore, while correlation coefficients near unity do not imply the lack of systematic error, we observe that models with higher correlation coefficients are associated with lower systematic errors, as reflected in mean deviations of lesser magnitude. The simultaneous convergence of the correlation coefficient, which depends on the relative adsorption affinities of the compounds, and the mean error, which depends on the mean affinity of all the

compounds, suggests that the best performing models could be associated with more realistic representations of the physicochemical environment of the adsorbates.

The experiments indicate that hydroxylation, with a few exceptions, reduces the affinity of the aromatics for the surface, with an average change of −0.6 in $\log_{10} K_i^{expt}$ values from naked to hydroxylated nanotubes. All of our simulations qualitatively agree with this observation; however, models graph−OH(A) and graph−OH(B) evidently reduce the affinity too much, as can be seen from the large negative mean deviations in Table 2. This reduction can be attributed to the OH groups sterically blocking the adsorbates from accessing the graphenic surface. Consistent with this, the free-energy minima for graph−OH(A) average 0.15 nm farther from the center of the graphene sheet than for naked graphene, occurring at distances of $0.49 \leq z \leq 0.55$ nm. The limited surface area available for adsorption on graph−OH(B) is clearly visible in Figure S3A. Thus, the uniform arrangement of OH at 2.4 nm^{-2} continues to underestimate the affinity for all compounds and to give mediocre correlation $r = 0.75$. The best performing uniform arrangement, shown in Figure 3C,
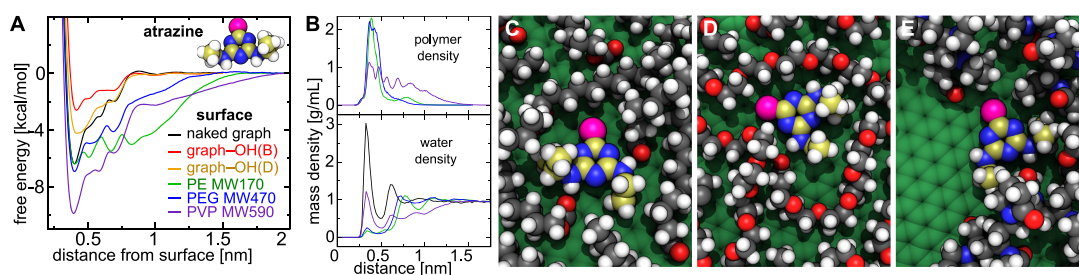
Figure 4. Adsorption of the herbacide atrazine on functionalized graphenic surfaces. (A) Free energy as a function of distance between an atrazine molecule and hydroxylated and polymer-conjugated graphene surfaces. The labels graph−OH(B) and graph−OH(D) refer to the OH arrangements in Figure 3B and D. For reference, the structure of the molecule is represented here with H, C, Cl, and N atoms shown as white, yellow, magenta, and blue spheres, respectively. **(B)** Mass density of polymer and water as a function of distance from the surface in the absence of atrazine. Black, green, blue, and purple lines correspond to naked, PE, PEG, and PVP systems. **(C, D, and E)** Representative simulation snapshots of atrazine adsorbed on graphene surfaces conjugated with PE, PEG, and PVP, respectively. For contrast, C atoms of the polymers and graphene are shown in gray and green, respectively.

gives a much improved correlation coefficient ($r = 0.87$), but in this case the OH density is 1.2 nm^{-2}, less than a quarter of that indicated by 3.70% OH content by weight.

Depending on the method of synthesis, OH groups might be expected to form hydrogen-bonding pairs or clusters on the nanotube surfaces.[96] The configuration in Figure 3D has an arrangement of pairs of OH groups with the same overall OH density as the configuration in Figure 3B. This simple modification of the graph−OH(B) arrangement changes the correlation between simulation and experiment from mediocre ($r = 0.76$) to excellent ($r = 0.93$). Furthermore, the paired arrangement yields an improvement in absolute terms, with the mean deviation $\langle \log_{10} K_i^{calc} \rangle - \langle \log_{10} K_i^{expt} \rangle$ changing from -1.9 for model graph−OH(B) to -0.47 for model graph−OH(D). While the OH density for this model (2.4 nm^{-2}) is still less than half the value suggested (5.6 nm^{-2}), we were not able to obtain a correlation > 0.8 nor a mean deviation of a similarly small magnitude attempting another arrangement with a density of 4.8 nm^{-2} (see Figure S12 in the SI). This apparent discrepancy in the OH densities may indicate an unrealistic design of the OH arrangement or carbon structure (oxidation-induced defects may be important[96]), an imbalance in the force field, or, perhaps, inaccuracy in the quoted value of OH content. Another possibility is that a significant fraction of OH groups are clustered near the end of the nanotube or at defects,[96,97] leaving most of the surface with a relatively low density of OH groups. Somewhat surprisingly, our results for model graph−OH(D) are in better agreement with experiment than those for the naked nanotube model. Interestingly, the structure−activity model[40] also correlated better with the hydroxylated nanotube experiments than those with the naked nanotube (0.96 vs 0.92).

Adsorption of Atrazine on Surface-Modified Carbon Nanotubes. The results above strongly suggest that molecular dynamics can make useful predictions of the adsorption affinity of small aromatics on carbon nanotubes and graphene-like surfaces. Hence, in this section, we apply the same techniques to take the first steps in optimizing the affinity of surface-modified graphenic carbon for the herbacide atrazine. Atrazine is a chlorinated aromatic compound possessing a 1,3,5-triazine ring and has substantial structural similarity with several other herbacides, such as simazine and cyromazine, as well as triazine dendrimers, which have been studied as delivery vehicles for cancer drugs.[98] A rendering of the molecule is included in Figure 4A.

We first considered the adsorption of atrazine on a naked graphene surface. As shown in Figure 4A, the potential of mean force is qualitatively similar to those considered previously (Figure 1B). Yan et al.[20] provides experimental characterization of the adsorption of atrazine on naked multiwall carbon nanotubes, which should be comparable to our calculated value. We can determine the adsorption equilibrium constant in the dilute limit from the fit of Yan et al. to the Langmuir model to give

$$\log_{10}(K^{expt}) = \log_{10}(K_L q_{max}) \qquad (6)$$

where K_L and q_{max} are parameters of the Langmuir model as defined by Yan et al.[20] and the units of the argument of the logarithm are converted to mL/g, consistent with the convention used thus far. Yan et al.[20] considered nanotubes of two different geometries and distinct synthesis techniques (specific surface areas of 167 and 300 m^2/g as determined by the Brunauer−Emmett−Teller method), as well as two temperatures (298 and 303 K) that straddle the temperature in our simulations (300 K). By eq 6, the experimental $\log_{10} K^{expt}$ values are 4.5 at 298 K and 4.3 at 303 K for the smaller nanotube and 5.2 at both temperatures for the larger nanotube. Part of the difference between these values for the larger and smaller nanotube is attributable to their different specific surface areas ($\log_{10}(300/167) \approx 0.25$); however, a discrepancy as large as 0.7 remains, which was ascribed to chemical or structural differences of unknown nature between the two types of nanotube.[20] From our potential of mean force (Figure 4A), we calculate $\log_{10} K^{calc}$ values of 2.7 and 2.9 for the smaller and

larger nanotubes, respectively; however, as can be seen from the mean deviation in Table 2, we systematically underestimate the adsorption equilibrium constant on naked carbon nanotubes by -0.92. It would therefore be reasonable to apply a correction of 0.9 to $\log_{10} K^{calc}$ for atrazine, to give a corrected values of 3.6 and 3.8, which might be considered acceptable agreement given the substantial variation in the experimental values for the different nanotubes.

Therefore, it is with some degree of confidence in the molecular dynamics description of atrazine adsorption that we study the effect of different surface modifications to graphenic carbon. We consider adsorption onto the hydroxylated graphene surfaces with the previously discussed arrangements shown in Figure 3B,D. As for the benzene derivatives, with atrazine, we find that hydroxylation generally reduces the adsorption affinity (see Figure 4A and Table 2). Quite distinct behavior is seen for our polymer-conjugated models, which comprise polyethylene (PE), polyethylene glycol (PEG), and polyvinylpyrrolidone (PVP) chains having molecular weights of 170, 470, and 580 Da attached *via* ester linkages to the graphene surface at areal densities of 1.20, 0.53, and 0.53 chains/nm^2, respectively. First, the fluctuating polymer brushes on average extend some distance from the surface; hence, as shown in Figure 4A, the potential of mean force is significantly less than zero even at distances greater than 1 nm from the surface, owing to intermittent interactions with the polymer brush at these distances. The extension of the polymer from the surface is quantified in Figure 4B, which plots both the mass density of polymer near the surface and the mass density of water, which is reduced on the polymer-conjugated surfaces. Furthermore, the simulations reveal hydrogen bonding between the NH groups of atrazine and oxygen atoms in the linker (see Figure S4C in the SI), as well as in the PEG and PVP chains. Examples of these hydrogen bonds are apparent in Figure 4C,D,E. Despite the favorable nature of these interactions, the global free-energy minimum remains associated with atrazine lying flat against the graphene surface, as it is for the naked surface. For reasons clarified below, the free-energy minima for PE- and PEG-conjugated graphene are only slightly deeper than for naked graphene, while atrazine adsorption on PVP-conjugated graphene is significantly more favorable than on any other surface considered here.

Molecular simulation gives reliable estimates of free energies, while simultaneously revealing atomic-level details of molecular interactions that would be difficult to probe with any experimental method. Thus, we not only find that our PVP-conjugated graphene surface yields a high affinity for atrazine but also identify the mechanism for its especially high affinity, which could inform further design of graphenic materials to optimize atrazine adsorption. A particularly important aspect of the polymer-conjugated systems is that the polymers themselves tend to adsorb to the surface, competing with the small-molecule adsorbates for space at the interface. PE and PEG, in particular, possess large peaks in density (Figure 4B) at the graphene interface and concomitant reductions in water density at this interface. As exemplified in Figure 4C,D, these two polymers form constantly reorganizing adsorbed monolayers on the graphene surface, atop which a transient second layer is sometimes formed. In contrast to these polymers, the PVP chains remain much more erect on the surface, leaving free space for both water and atrazine to adsorb (Figure 4E). Although the density of water at the PVP-conjugated surface is less than for the naked surface, nearly a third of the surface remains uncovered for the PVP density considered here. The distinct behavior of PVP as compared to the other polymers is due to PVP's greater stiffness and bulkier geometry, making it difficult for the PVP chains to bend toward the surface and pack there. For instance, PVP is much more rigid than PEG, possessing a persistence length of 0.67 nm in the isotactic form,[99] while PEG's persistence length[100] is about 0.37 nm. Thus, while all three polymers form favorable interactions with atrazine, only PVP is able to do this without strongly competing with atrazine for the graphene surface.

CONCLUSION

As validation of the molecular dynamics approach to nanomaterial design, we have shown that simulation reliably predicts relative adsorption affinities of a range of small aromatics on naked and hydroxylated nanotubes, a feat that cannot be accomplished by simple models, such as those considering only the octanol–water partition coefficient. Molecular simulation may also help in the determination of the atomic-scale structure of nanomaterial surfaces by comparison, to experimental data, of simulation results for multiple atomistic models, exemplified in our exploration of different hydroxylated nanotube models. Moreover, using atrazine as an example, we have illustrated the invaluable insight that can be obtained from simulation for engineering materials with high affinities for particular adsorbates.

Implicit in the agreement we found between experiment and simulation is the basic validity of the CHARMM general force field[101] for describing interactions between the atoms of the system. However, despite the high correlation between the experiment and simulation, molecular dynamics predictions must still be regarded as semiquantitative. Notably, the predicted concentrations at the surface are an order of magnitude too small for naked graphene. The affinity of atrazine for the naked surface also appeared to be underestimated, even after making an empirical correction to $\log_{10} K_i^{calc}$ based on our results for the other compounds.

There are several possible factors that could contribute to the discrepancy between the experimental and calculated results. It is very likely that some the disagreement is due to imperfections in the force field and water model. The graphene–water interface possesses a very sharp change in dielectric properties, which is known to be a point of failure for fixed-charge atomic models;[82] thus, some explicit treatment of electronic polarizability may be necessary.[70,85] Some of the discrepancy may even be inherent to the classical molecular dynamics approach, which is incapable of fully describing quantum chemical systems. On the other hand, poor convergence of the free energy calculations or lack of adequate sampling could yield unreliable results; however, this is unlikely given the validation detailed in Figures S1–4. As shown in Figures S5–9 and Table S1 in the SI, we have also considered several aspects of the simulation protocol, all of which appear to be negligible compared to the deviation between experiment and simulation. Due to the low surface concentrations in experiment, it appears that the discrepancy cannot be explained by interactions between adsorbed molecules; however, the presence of unknown adsorbed contaminants may have similar effects to those seen on surfaces with substantial loading (see Figure 2).

While the present work has, to some extent, validated existing atomistic models of graphenic and modified graphenic surfaces, there has been little systematic evaluation of models used for other nanomaterials. Existing force fields for materials such as metals and ceramics may require further evaluation to demonstrate whether they perform consistently for a wide variety of organic adsorbates. Moreover, many exciting new materials lack any force fields with even minimal validation. On the experimental side, more consistent synthesis and better characterization can also help in constructing more accurate models.

The experimental data used in the present work were originally obtained to construct a surface adsorption index[38–40] that relates adsorbate physicochemical properties to their affinity for nanomaterial surfaces. We have shown here that, in some cases, this surface adsorption index could be constructed more conveniently *in silico*. While molecular dynamics can directly yield adsorption free energies, such calculations become rapidly more expensive and time-consuming as the systems become larger and more complicated. Therefore, we recognize the potential of combining information gleaned from simulation with a structure–activity approach exemplified by the surface adsorption index. The optimal strategy may be a multiscale approach, using explicit-solvent molecular dynamics and coarser descriptions derived from it, such as the grand-canonical Monte Carlo/Brownian dynamics approach, to build predictive structure–activity models for complex heterogeneous systems.

METHODS

Adsorbate Models. Structures of atrazine and the molecules listed in Table 1 were obtained from ChemSpider[102] and converted to mol2 format using Open Babel.[103] The molecules were parametrized in accordance with CGenFF,[101] version 2b8, using the ParamChem Web interface (CGenFF program version 0.9.7.1 beta).[104,105] The penalties reported by the CGenFF program, indicating the reliability of the generated parameters, were zero in most cases and surpassed 10 (meaning "some validation may be required") only for phenyl acetate, phenylethanol, and methyl-2-methyl benzoate. Atrazine also gave a particularly high penalty; however, as discussed in the Results and Discussion, the deviation of the equilibrium constant adsorption on carbon nanotubes from experiment[20] was not considerably larger than for the other compounds.

Unmodified Multiwall Carbon Nanotube Model. Four layers of graphene in a graphite arrangement were generated using the InorganicBuilder plugin[106,107] of VMD.[108] Each layer was a supercell of the graphene lattice, with the form of a regular hexagon of side length 1.702 nm. The layers were periodically continued throughout in the xy plane, forming an effectively infinite flat surface. After adding 758 water molecules above and below the membrane, the systems had the form of a hexagonal prism, with an equilibrium (at $T = 300$ K and $P = 1$ atm) height of ~4.4 nm. A representation of one such system is shown in Figure 1A. For convenience, weak harmonic restraints kept the carbon atoms near their initial positions. Although these restraints have a negligible effect on the calculated free energy (<0.15 kcal/mol), we have subsequently found them to be unnecessary and do not recommend their use in future simulations. See Figure S7 in the SI for a discussion.

Hydroxylated Multiwall Carbon Nanotube Models. Beginning with the four-layer graphite model above, we generated five models of hydroxylated graphenic carbon with different densities and arrangements of hydroxyl groups. To yield homogeneous surfaces that could be more easily sampled in the free-energy calculations, we placed the hydroxyl groups so that the system's cross section in the xy plane was an exact supercell of identical tiled subcells. The configurations of the systems are summarized in Table 2 and illustrated in Figure 3. The first three systems, denoted graph–OH(A), (B), and (C), had 72, 18, and 9 uniformly spaced hydroxyl groups. The fourth system, denoted graph–OH(D), had the same arrangement as graph–OH(C) except that a second hydroxyl group was added at the 4-position of the first hydroxyl's six-membered ring. Thus, the two adjacent hydroxyl groups formed hydrogen-bonding pairs. A fifth system was created with 36 OH groups arranged in clusters of effectively infinite lines; the results for this model are available in Figure S12 in the SI. Atomic charges, Lennard-Jones parameters, and bonded parameters were assigned to the hydroxyl groups and associated carbon atom by analogy to the CGenFF parametrization of *tert*-butanol. Notably, the hydrogen, oxygen, and attached carbon atoms were assigned charges of $0.419e$, $-0.65e$, and $0.228e$, respectively. For charge neutralization, the three graphenic carbons bonded to the modified carbon were given charges of $0.001e$. Harmonic restraints (see Figure S7 in the SI) were applied only to unsubstituted carbon atoms so that the hydroxylated carbon atoms adopted a somewhat tetrahedral arrangement.

Polymer-Conjugated Nanotube Models. We constructed models of methyl-terminated PE, PEG, and PVP with molecular weights of about 170, 470, and 590 Da, respectively. The carefully calibrated PEG CHARMM force field[100] was used for that polymer, while CGenFF was used for the other two. The parameters for PE should be reliable, as they are identical to those in alkyl chains of CHARMM lipids and proteins. The CGenFF program[104,105] indicated relatively high penalties for the PVP molecule, so this model

may be more approximate. The PVP molecule was generated in an isotactic configuration. To represent realistic surface conjugation of carbon nanotubes, 4 or 9 carboxylate groups were first covalently attached to the upper graphene sheet shown in Figure 1A. As with the addition of hydroxyl groups, the carboxylate groups were placed so as to be repeated subcells within the system's periodic cell. Three systems were created, covalently linking the carboxylates to 9 PE, 4 PEG, or 4 PVP fragments. Beginning from the bond attaching the carboxylate to the graphene surface, the resulting structures were $-C(=O)OC_{11}$, $-C(=O)OC(COC)_{11}CH_3$, and $-C(=O)OC[C(-Py)C]_5CH_3$, where Py is the 2-pyrrolidone group. Force field parameters for the linker were derived from a CGenFF model of butyl pivalate. The polymer chains extended some distance from the surface; thus, an additional layer of water was added along the z axis to prevent spurious interaction between periodic images, giving an average z dimension of about 6.8 nm and increasing the number of water molecules in the system to about 1250. For the naked graphene surface, calculations were performed both with the four-layer model as shown in Figure 1A and with a single-layer model. As shown in Figure S1 in the SI, the difference in the potentials of mean force was detectable, but small enough to be irrelevant compared to other factors in comparison to experiment. All other calculations for atrazine included only a single modified graphene layer.

Molecular Dynamics Simulations. All simulations were executed in the molecular dynamics software NAMD 2.10[109] using computing resources maintained by Kansas State University, as well as those supplied through the Extreme Science and Engineering Discovery Environment (XSEDE).[110] All simulations employed the standard TIP3P water model used by the CHARMM force field. The temperature and pressure were maintained at 300 K and 101.325 kPa, respectively, by the Langevin thermostat and Langevin piston[111] methods. The area of the systems was fixed in the xy plane, and the Langevin piston acted only along the z axis. As shown in Figure S5 in the SI, no significant differences were seen between an exemplary free-energy calculation employing a smooth $0.8-0.9$ nm cutoff of van der Waals forces and another with the more conventional $1.0-1.2$ nm cutoff; thus, the former cutoff scheme was chosen for efficiency. Electrostatic interactions were computed via the particle-mesh Ewald algorithm,[112] with a mesh spacing of <0.12 nm. The length of covalent bonds involving hydrogen atoms was constrained[113,114] to the values prescribed by the CHARMM force field. The equations of motion were integrated using a multiple time-stepping scheme[115] with steps of 2 and 4 fs for short- and long-range interactions. VMD 1.9.2 was used for analysis and visualization.[108]

Free-Energy Calculations. For each surface model considered, $29-32$ independent systems were constructed, each containing a different adsorbate molecule. Each system underwent 2000 steps of energy minimization followed by 20 ps of equilibration before beginning the free-energy calculation. The adaptive biasing force[59,87,88] method was applied to the z component of the vector between the center of mass of the adsorbate and center of mass of atoms of the first surface layer of the nanomaterial, using the Colvars module[116] of NAMD 2.10. The motion of the adsorbates in the xy plane was not restricted, and they sampled a variety of lateral positions and orientations during the simulations (see Figures S2–4 in the SI). Unless otherwise stated, the calculations were performed using a single window on the interval $0.3 \leq z \leq 1.5$ nm, and force samples were collected in bins having widths of 0.005 nm to capture small-scale variations in the potential of mean force. All calculations were performed using the simulation conditions described in the section Molecular Dynamics Simulations for $300-600$ ns of simulated time. Convergence of the calculations is detailed in Figure S1 of the SI. Plotted potentials of mean force were anchored so that the mean value on $1.45 \leq z \leq 1.5$ nm was zero. Equation 4 was applied with $c = 0.8$ nm, although the precise value was irrelevant (see Figure S3 in the SI). As an additional check, we performed free-energy perturbation[117] for the three systems to verify the ΔG of adsorption (see Table S1 in the SI).

The free-energy calculations for atrazine on polymer-conjugated surfaces were performed slightly differently than above. To equilibrate the polymer chains, the systems were first simulated for 50 ns in the absence of atrazine. Because of the extension of the polymers from the surface, a greater distance from the surface z was required to reach the plateau of $w_i^{calc}(z)$; thus, the free-energy calculations for the polymer-conjugated surfaces were performed in two overlapping windows, $0.3 \leq z \leq 1.2$ nm and $1.0 \leq z \leq 2.0$ nm. Due to the flexibility of the polymers and the greater conformational space that needed to be sampled (see Figure S4 in the SI), these calculations employed multiple-walker adaptive biasing force[118] using 3 walkers for each window and a simulated time of 200 ns per walker per window (totaling 1.2 μs per system).

Conflict of Interest: The authors declare no competing financial interest.

REFERENCES AND NOTES

1. Petros, R. A.; DeSimone, J. M. Strategies in the Design of Nanoparticles for Therapeutic Applications. *Nat. Rev. Drug Discovery* **2010**, *9*, 615–627.
2. Parveen, S.; Misra, R.; Sahoo, S. K. Nanoparticles: a Boon to Drug Delivery, Therapeutics, Diagnostics and Imaging. *Nanomedicine* **2012**, *8*, 147–166.
3. Wang, A. Z.; Langer, R.; Farokhzad, O. C. Nanoparticle Delivery of Cancer Drugs. *Annu. Rev. Med.* **2012**, *63*, 185–198.
4. Lynch, I.; Cedervall, T.; Lundqvist, M.; Cabaleiro-Lago, C.; Linse, S.; Dawson, K. A. The Nanoparticle-Protein Complex as a Biological Entity; A Complex Fluids and Surface Science Challenge for the 21st Century. *Adv. Colloid Interface Sci.* **2007**, *134*, 167–174.
5. Röcker, C.; Pötzl, M.; Zhang, F.; Parak, W. J.; Nienhaus, G. U. A Quantitative Fluorescence Study of Protein Monolayer Formation on Colloidal Nanoparticles. *Nat. Nanotechnol.* **2009**, *4*, 577–580.
6. Tenzer, S.; Docter, D.; Rosfa, S.; Wlodarski, A.; Kuharev, J.; Rekik, A.; Knauer, S. K.; Bantz, C.; Nawroth, T.; Bier, C.; et al. Nanoparticle Size Is a Critical Physicochemical Determinant of the Human Blood Plasma Corona: a Comprehensive Quantitative Proteomic Analysis. *ACS Nano* **2011**, *5*, 7155–7167.
7. Monteiro-Riviere, N. A.; Samberg, M. E.; Oldenburg, S. J.; Riviere, J. E. Protein Binding Modulates the Cellular Uptake of Silver Nanoparticles into Human Cells: Implications for in vitro to in vivo Extrapolations? *Toxicol. Lett.* **2013**, *220*, 286–293.
8. Sasidharan, A.; Riviere, J. E.; Monteiro-Riviere, N. Gold and Silver Nanoparticle Interactions with Human Proteins: Impact and Implications in Biocorona Formation. *J. Mater. Chem. B* **2015**, *3*, 2075–2082.
9. Monopoli, M. P.; Åberg, C.; Salvati, A.; Dawson, K. A. Biomolecular Coronas Provide the Biological Identity of Nanosized Materials. *Nat. Nanotechnol.* **2012**, *7*, 779–786.

10. Riviere, J. E. Of Mice, Men and Nanoparticle Biocoronas: Are *in vitro* to *in vivo* Correlations and Interspecies Extrapolations Realistic? *Nanomedicine* **2013**, *8*, 1357–1359.

11. Dobrovolskaia, M. A.; McNeil, S. E. Immunological Properties of Engineered Nanomaterials. *Nat. Nanotechnol.* **2007**, *2*, 469–478.

12. Zolnik, B. S.; González-Fernández, Á; Sadrieh, N.; Dobrovolskaia, M. A. Minireview: Nanoparticles and the Immune System. *Endocrinology* **2010**, *151*, 458–465.

13. Syed, S.; Zubair, A.; Frieri, M. Immune Response to Nanomaterials: Implications for Medicine and Literature Review. *Curr. Allergy Asthma Rep.* **2013**, *13*, 50–57.

14. Dobrovolskaia, M. A.; Patri, A. K.; Zheng, J.; Clogston, J. D.; Ayub, N.; Aggarwal, P.; Neun, B. W.; Hall, J. B.; McNeil, S. E. Interaction of Colloidal Gold Nanoparticles with Human Blood: Effects on Particle Size and Analysis of Plasma Protein Binding Profiles. *Nanomedicine* **2009**, *5*, 106–117.

15. Dobrovolskaia, M. A.; Patri, A. K.; Potter, T. M.; Rodriguez, J. C.; Hall, J. B.; McNeil, S. E. Dendrimer-induced Leukocyte Procoagulant Activity Depends on Particle Size and Surface Charge. *Nanomedicine* **2012**, *7*, 245–256.

16. Bucak, S.; Jones, D. A.; Laibinis, P. E.; Hatton, T. A. Protein Separations Using Colloidal Magnetic Nanoparticles. *Biotechnol. Prog.* **2003**, *19*, 477–484.

17. Ma, C.; Li, C.; He, N.; Wang, F.; Ma, N.; Zhang, L.; Lu, Z.; Ali, Z.; Xi, Z.; Li, X.; et al. Preparation and Characterization of Monodisperse Core-shell Fe3O4@SiO2Microspheres and Its Application for Magnetic Separation of Nucleic Acids from E. Coli BL21. *J. Biomed. Nanotechnol.* **2012**, *8*, 1000–1005.

18. Cano, M.; Sbargoud, K.; Allard, E.; Larpent, C. Magnetic Separation of Fatty Acids with Iron Oxide Nanoparticles and Application to Extractive Deacidification of Vegetable Oils. *Green Chem.* **2012**, *14*, 1786–1795.

19. Cromer, J. R.; Wood, S. J.; Miller, K. A.; Nguyen, T.; David, S. A. Functionalized Dendrimers as Endotoxin Sponges. *Bioorg. Med. Chem. Lett.* **2005**, *15*, 1295–1298.

20. Yan, X.; Shi, B.; Lu, J.; Feng, C.; Wang, D.; Tang, H. Adsorption and Desorption of Atrazine on Carbon Nanotubes. *J. Colloid Interface Sci.* **2008**, *321*, 30–38.

21. Morin, G.; Wang, Y.; Ona-Nguema, G.; Juillot, F.; Calas, G.; Menguy, N.; Aubry, E.; Bargar, J. R.; Brown, G. E., Jr EXAFS and HRTEM Evidence for As(III)-containing Surface Precipitates on Nanocrystalline Magnetite: Implications for As Sequestration. *Langmuir* **2009**, *25*, 9119–9128.

22. Yavuz, C. T.; Mayo, J.; Suchecki, C.; Wang, J.; Ellsworth, A. Z.; DCouto, H.; Quevedo, E.; Prakash, A.; Gonzalez, L.; Nguyen, C.; et al. Pollution Magnet: Nano-magnetite for Arsenic Removal from Drinking Water. *Environ. Geochem. Health* **2010**, *32*, 327–334.

23. Che, B. H. X.; Yeap, S. P.; Ahmad, A. L.; Lim, J. Layer-by-layer Assembly of Iron Oxide Magnetic Nanoparticles Decorated Silica Colloid for Water Remediation. *Chem. Eng. J.* **2014**, *243*, 68–78.

24. Ravelo-Pérez, L. M.; Herrera-Herrera, A. V.; Hernández-Borges, J.; Rodríguez-Delgado, M. Á Carbon Nanotubes: Solid-phase Extraction. *J. Chromatogr. A* **2010**, *1217*, 2618–2641.

25. Pyrzynska, K. Carbon Nanotubes as Sorbents in the Analysis of Pesticides. *Chemosphere* **2011**, *83*, 1407–1413.

26. Zhu, Y.-Z.; Zhao, M.-A.; Nan Feng, Y.; Han Kim, J. Multiresidue Method for the Determination of 227 Pesticides in Hot Pepper (Capsicum Annuum L.) by Liquid Chromatography with Tandem Mass Spectrometry. *J. Sep. Sci.* **2014**, *37*, 2947–2954.

27. Zhou, Q.; Xiao, J.; Wang, W.; Liu, G.; Shi, Q.; Wang, J. Determination of Atrazine and Simazine in Environmental Water Samples Using Multiwalled Carbon Nanotubes as the Adsorbents for Preconcentration Prior to High Performance Liquid Chromatography with Diode Array Detector. *Talanta* **2006**, *68*, 1309–1315.

28. El-Sheikh, A. H.; Insisi, A. A.; Sweileh, J. A. Effect of Oxidation and Dimensions of Multi-walled Carbon Nanotubes on Solid Phase Extraction and Enrichment of Some Pesticides from Environmental Waters Prior to Their Simultaneous Determination by High Performance Liquid Chromatography. *J. Chromatogr. A* **2007**, *1164*, 25–32.

29. Walters, W. P.; Stahl, M. T.; Murcko, M. A. Virtual Screening—an Overview. *Drug Discovery Today* **1998**, *3*, 160–178.

30. Lyne, P. D. Structure-based Virtual Screening: an Overview. *Drug Discovery Today* **2002**, *7*, 1047–1055.

31. Kitchen, D. B.; Decornez, H.; Furr, J. R.; Bajorath, J. Docking and Scoring in Virtual Screening for Drug Discovery: Methods and Applications. *Nat. Rev. Drug Discovery* **2004**, *3*, 935–949.

32. Jorgensen, W. L. The Many Roles of Computation in Drug Discovery. *Science* **2004**, *303*, 1813–1818.

33. Chodera, J. D.; Mobley, D. L.; Shirts, M. R.; Dixon, R. W.; Branson, K.; Pande, V. S. Alchemical Free Energy Methods for Drug Discovery: Progress and Challenges. *Curr. Opin. Struct. Biol.* **2011**, *21*, 150–160.

34. Li, M.; Al-Jamal, K. T.; Kostarelos, K.; Reineke, J. Physiologically Based Pharmacokinetic Modeling of Nanoparticles. *ACS Nano* **2010**, *4*, 6303–6317.

35. Nel, A.; Xia, T.; Meng, H.; Wang, X.; Lin, S.; Ji, Z.; Zhang, H. Nanomaterial Toxicity Testing in the 21st Century: Use of a Predictive Toxicological Approach and High-throughput Screening. *Acc. Chem. Res.* **2013**, *46*, 607–621.

36. Melagraki, G.; Afantitis, A. Enalos InSilicoNano Platform: an Online Decision Support Tool for the Design and Virtual Screening of Nanoparticles. *RSC Adv.* **2014**, *4*, 50713–50725.

37. Fourches, D.; Pu, D.; Tassa, C.; Weissleder, R.; Shaw, S. Y.; Mumper, R. J.; Tropsha, A. Quantitative Nanostructure-Activity Relationship Modeling. *ACS Nano* **2010**, *4*, 5703–5712.

38. Xia, X.-R.; Monteiro-Riviere, N. A.; Riviere, J. E. An Index for Characterization of Nanomaterials in Biological Systems. *Nat. Nanotechnol.* **2010**, *5*, 671–675.

39. Xia, X. R.; Monteiro-Riviere, N. A.; Mathur, S.; Song, X.; Xiao, L.; Oldenberg, S. J.; Fadeel, B.; Riviere, J. E. Mapping the Surface Adsorption Forces of Nanomaterials in Biological Systems. *ACS Nano* **2011**, *5*, 9074–9081.

40. Chen, R.; Zhang, Y.; Darabi Sahneh, F.; Scoglio, C. M.; Wohlleben, W.; Haase, A.; Monteiro-Riviere, N. A.; Riviere, J. E. Nanoparticle Surface Characterization and Clustering through Concentration-Dependent Surface Adsorption Modeling. *ACS Nano* **2014**, *8*, 9446–9456.

41. Slocik, J. M.; Naik, R. R. Probing Peptide-nanomaterial Interactions. *Chem. Soc. Rev.* **2010**, *39*, 3454–3463.

42. Heinz, H.; Farmer, B. L.; Pandey, R. B.; Slocik, J. M.; Patnaik, S. S.; Pachter, R.; Naik, R. R. Nature of Molecular Interactions of Peptides with Gold, Palladium, and Pd-Au Bimetal Surfaces in Aqueous Solution. *J. Am. Chem. Soc.* **2009**, *131*, 9704–9714.

43. Coppage, R.; Slocik, J. M.; Briggs, B. D.; Frenkel, A. I.; Heinz, H.; Naik, R. R.; Knecht, M. R. Crystallographic Recognition Controls Peptide Binding for Bio-Based Nanomaterials. *J. Am. Chem. Soc.* **2011**, *133*, 12346–12349.

44. Heinz, H.; Lin, T.-J.; Kishore Mishra, R.; Emami, F. S. Thermodynamically Consistent Force Fields for the Assembly of Inorganic, Organic, and Biological Nanostructures: the INTERFACE Force Field. *Langmuir* **2013**, *29*, 1754–1765.

45. Katoch, J.; Kim, S. N.; Kuang, Z.; Farmer, B. L.; Naik, R. R.; Tatulian, S. A.; Ishigami, M. Structure of a Peptide Adsorbed on Graphene and Graphite. *Nano Lett.* **2012**, *12*, 2342–2346.

46. Maiti, P.; Bagchi, B. Structure and Dynamics of DNA-dendrimer Complexation: Role of Counterions, Water, and Base Pair Sequence. *Nano Lett.* **2006**, *6*, 2478–2485.

47. Vasumathi, V.; Maiti, P. Complexation of siRNA with Dendrimer: A Molecular Modeling Approach. *Macromolecules* **2010**, *43*, 8264–8274.

48. Maingi, V.; Kumar, M. V. S.; Maiti, P. K. PAMAM Dendrimer-drug Interactions: Effect of pH on the Binding and Release Pattern. *J. Phys. Chem. B* **2012**, *116*, 4370–4376.

49. Vergara-Jaque, A.; Comer, J.; Monsalve, L.; González-Nilo, F. D.; Sandoval, C. A Computationally Efficient Methodology for Atomic-Level Characterization of Dendrimer-Drug Complexes: A Comparison of Amine- and Acetyl-Terminated PAMAM. *J. Phys. Chem. B* **2013**, *117*, 6801–6813.

50. Carrasco-Sánchez, V.; Vergara-Jaque, A.; Zuñiga, M.; Comer, J.; John, A.; Nachtigall, F. M.; Valdes, O.; Duran-Lara, E. F.; Sandoval, C.; Santos, L. S. In Situ and in Silico Evaluation of Amine-and Folate-terminated Dendrimers as Nanocarriers of Anesthetics. *Eur. J. Med. Chem.* **2014**, *73*, 250–257.

51. Vilos, C.; Morales, F. A.; Solar, P. A.; Herrera, N. S.; Gonzalez-Nilo, F. D.; Aguayo, D. A.; Mendoza, H. L.; Comer, J.; Bravo, M. L.; Gonzalez, P. A.; et al. Paclitaxel-PHBV Nanoparticles and Their Toxicity to Endometrial and Primary Ovarian Cancer Cells. *Biomaterials* **2013**, *34*, 4098–4108.

52. Sun, C.; Tang, T.; Uludag, H. A Molecular Dynamics Simulation Study on the Effect of Lipid Substitution on Polyethylenimine Mediated siRNA Complexation. *Biomaterials* **2013**, *34*, 2822–2833.

53. Brancolini, G.; Kokh, D. B.; Calzolai, L.; Wade, R. C.; Corni, S. Docking of Ubiquitin to Gold Nanoparticles. *ACS Nano* **2012**, *6*, 9863–9878.

54. Carr, R.; Comer, J.; Ginsberg, M. D.; Aksimentiev, A. Modeling Pressure-Driven Transport of Proteins through a Nanochannel. *IEEE Trans. Nanotechnol.* **2011**, *10*, 75–82.

55. Kollman, P. Free Energy Calculations: Applications to Chemical and Biochemical Phenomena. *Chem. Rev.* **1993**, *93*, 2395–2417.

56. Jorgensen, W. L. Free Energy Calculations: a Breakthrough for Modeling Organic Chemistry in Solution. *Acc. Chem. Res.* **1989**, *22*, 184–189.

57. Chipot, C.; Pohorille, A. *Free Energy Calculations*; Springer: Berlin, 2007.

58. Barducci, A.; Bonomi, M.; Parrinello, M. Metadynamics. *Wiley Interdiscip. Rev. Comput. Mol. Sci.* **2011**, *1*, 826–843.

59. Comer, J.; Gumbart, J. C.; Hénin, J.; Lelièvre, T.; Pohorille, A.; Chipot, C. The Adaptive Biasing Force Method. Everything You Always Wanted to Know, But Were Afraid to Ask. *J. Phys. Chem. B* **2015**, *119*, 1129–1151.

60. Woo, H.-J.; Roux, B. Calculation of Absolute Protein-ligand Binding Free Energy from Computer Simulations. *Proc. Natl. Acad. Sci. U. S. A.* **2005**, *102*, 6825–6830.

61. Gumbart, J. C.; Roux, B.; Chipot, C. Standard Binding Free Energies from Computer Simulations: What Is the Best Strategy? *J. Chem. Theory Comput.* **2013**, *9*, 794–802.

62. Gumbart, J. C.; Roux, B.; Chipot, C. Efficient Determination of Protein-protein Standard Binding Free Energies from First Principles. *J. Chem. Theory Comput.* **2013**, *9*, 3789–3798.

63. Limongelli, V.; Bonomi, M.; Parrinello, M. Funnel Metadynamics as Accurate Binding Free-energy Method. *Proc. Natl. Acad. Sci. U. S. A.* **2013**, *110*, 6358–6363.

64. Hoefling, M.; Iori, F.; Corni, S.; Gottschalk, K.-E. Interaction of Amino Acids with the Au (111) Surface: Adsorption Free Energies from Molecular Dynamics Simulations. *Langmuir* **2010**, *26*, 8347–8351.

65. Vila Verde, A.; Beltramo, P. J.; Maranas, J. K. Adsorption of Homopolypeptides on Gold Investigated Using Atomistic Molecular Dynamics. *Langmuir* **2011**, *27*, 5918–5926.

66. Di Felice, R.; Corni, S. Simulation of Peptide-surface Recognition. *J. Phys. Chem. Lett.* **2011**, *2*, 1510–1519.

67. Nawrocki, G.; Cieplak, M. Aqueous Amino Acids and Proteins Near the Surface of Gold in Hydrophilic and Hydrophobic Force Fields. *J. Phys. Chem. C* **2014**, *118*, 12929–12943.

68. Hughes, Z. E.; Wright, L. B.; Walsh, T. R. Biomolecular Adsorption at Aqueous Silver Interfaces: First-principles Calculations, Polarizable Force-field Simulations, and Comparisons with Gold. *Langmuir* **2013**, *29*, 13217–13229.

69. Nawrocki, G.; Cieplak, M. Amino Acids and Proteins at ZnO-water Interfaces in Molecular Dynamics Simulations. *Phys. Chem. Chem. Phys.* **2013**, *15*, 13628–13636.

70. Hughes, Z. E.; Tomásio, S. M.; Walsh, T. R. Efficient Simulations of the Aqueous Bio-interface of Graphitic Nanostructures with a Polarisable Model. *Nanoscale* **2014**, *6*, 5438–5448.

71. Hughes, Z. E.; Walsh, T. R. What Makes a Good Graphene-binding Peptide? Adsorption of Amino Acids and Peptides at Aqueous Graphene Interfaces. *J. Mater. Chem. B* **2015**, *3*, 3211–3221.

72. Carr, R.; Comer, J.; Ginsberg, M. D.; Aksimentiev, A. Microscopic Perspective on the Adsorption Isotherm of a Heterogeneous Surface. *J. Phys. Chem. Lett.* **2011**, *2*, 1804–1807.

73. Johnson, R. R.; Kohlmeyer, A.; Johnson, A. C.; Klein, M. L. Free Energy Landscape of a DNA-carbon Nanotube Hybrid Using Replica Exchange Molecular Dynamics. *Nano Lett.* **2009**, *9*, 537–541.

74. Johnson, R. R.; Johnson, A.; Klein, M. L. The Nature of DNA-Base-Carbon-Nanotube Interactions. *Small* **2010**, *6*, 31–34.

75. Lin, S.; Hilmer, A. J.; Mendenhall, J. D.; Strano, M. S.; Blankschtein, D. Molecular Perspective on Diazonium Adsorption for Controllable Functionalization of Single-walled Carbon Nanotubes in Aqueous Surfactant Solutions. *J. Am. Chem. Soc.* **2012**, *134*, 8194–8204.

76. Ulissi, Z. W.; Zhang, J.; Sresht, V.; Blankschtein, D.; Strano, M. S. 2D Equation-of-State Model for Corona Phase Molecular Recognition on Single-Walled Carbon Nanotube and Graphene Surfaces. *Langmuir* **2015**, *31*, 628–636.

77. Bradley, R. H.; Cassity, K.; Andrews, R.; Meier, M.; Osbeck, S.; Andreu, A.; Johnston, C.; Crossley, A. Surface Studies of Hydroxylated Multi-wall Carbon Nanotubes. *Appl. Surf. Sci.* **2012**, *258*, 4835–4843.

78. Gammon, D. W.; Aldous, C. N.; Carr, W. C.; Sanborn, J. R.; Pfeifer, K. F. A Risk Assessment of Atrazine Use in California: Human Health and Ecological Aspects. *Pest Manage. Sci.* **2005**, *61*, 331–355.

79. Wells, D.; Belkin, M.; Comer, J.; Aksimentiev, A. Assessing Graphene Nanopores for Sequencing DNA. *Nano Lett.* **2012**, *12*, 4117–4123.

80. MacKerell, A. D., Jr.; Bashford, D.; Bellott, M.; Dunbrack, R. L., Jr.; Evanseck, J. D.; Field, M. J.; Fischer, S.; Gao, J.; Guo, H.; Ha, S.; et al. All-atom Empirical Potential for Molecular Modeling and Dynamics Studies of Proteins. *J. Phys. Chem. B* **1998**, *102*, 3586–3616.

81. Ponder, J. W.; Wu, C.; Ren, P.; Pande, V. S.; Chodera, J. D.; Schnieders, M. J.; Haque, I.; Mobley, D. L.; Lambrecht, D. S.; DiStasio, R. A., Jr; et al. Current Status of the AMOEBA Polarizable Force Field. *J. Phys. Chem. B* **2010**, *114*, 2549–2564.

82. Huang, J.; Lopes, P. E.; Roux, B.; MacKerell, A. D., Jr Recent Advances in Polarizable Force Fields for Macromolecules: Microsecond Simulations of Proteins Using the Classical Drude Oscillator Model. *J. Phys. Chem. Lett.* **2014**, *5*, 3144–3150.

83. Wu, J. C.; Chattree, G.; Ren, P. Automation of AMOEBA Polarizable Force Field Parameterization for Small Molecules. *Theor. Chem. Acc.* **2012**, *131*, 1–11.

84. Huang, L.; Roux, B. Automated Force Field Parameterization for Nonpolarizable and Polarizable Atomic Models Based on Ab Initio Target Data. *J. Chem. Theory Comput.* **2013**, *9*, 3543–3556.

85. Ho, T. A.; Striolo, A. Polarizability Effects in Molecular Dynamics Simulations of the Graphene-water Interface. *J. Chem. Phys.* **2013**, *138*, 054117.

86. Vanommeslaeghe, K.; MacKerell, A. CHARMM Additive and Polarizable Force Fields for Biophysics and Computer-aided Drug Design. *Biochim. Biophys. Acta, Gen. Subj.* **2015**, *1850*, 861–871.

87. Darve, E.; Pohorille, A. Calculating Free Energies Using Average Force. *J. Chem. Phys.* **2001**, *115*, 9169–9183.

88. Hénin, J.; Chipot, C. Overcoming Free Energy Barriers Using Unconstrained Molecular Dynamics Simulations. *J. Chem. Phys.* **2004**, *121*, 2904–2914.

89. Leenaerts, O.; Partoens, B.; Peeters, F. Water on Graphene: Hydrophobicity and Dipole Moment Using Density Functional Theory. *Phys. Rev. B: Condens. Matter Mater. Phys.* **2009**, *79*, 235440.

90. Schulten, K.; Schulten, Z.; Szabo, A. Dynamics of Reactions Involving Diffusive Barrier Crossing. *J. Chem. Phys.* **1981**, *74*, 4426–4432.

91. Comer, J. R.; Chipot, C. J.; Gonzalez-Nilo, F. D. Calculating Position-dependent Diffusivity in Biased Molecular Dynamics Simulations. *J. Chem. Theory Comput.* **2013**, *9*, 876–882.

92. Chen, W.; Duan, L.; Zhu, D. Adsorption of Polar and Nonpolar Organic Chemicals to Carbon Nanotubes. *Environ. Sci. Technol.* **2007**, *41*, 8295–8300.

93. Chen, W.; Duan, L.; Wang, L.; Zhu, D. Adsorption of Hydroxyl-and Amino-substituted Aromatics to Carbon Nanotubes. *Environ. Sci. Technol.* **2008**, *42*, 6862–6868.

94. Johnson, R. R.; Johnson, A. C.; Klein, M. L. Probing the Structure of DNA-carbon Nanotube Hybrids with Molecular Dynamics. *Nano Lett.* **2008**, *8*, 69–75.

95. Im, W.; Seefeld, S.; Roux, B. A Grand Canonical Monte Carlo-Brownian Dynamics Algorithm for Simulating Ion Channels. *Biophys. J.* **2000**, *79*, 788–801.

96. Ghaderi, N.; Peressi, M. First-principle Study of Hydroxyl Functional Groups on Pristine, Defected Graphene, and Graphene Epoxide. *J. Phys. Chem. C* **2010**, *114*, 21625–21630.

97. Robinson, J. A.; Snow, E. S.; Badescu, S. C.; Reinecke, T. L.; Perkins, F. K. Role of Defects in Single-walled Carbon Nanotube Chemical Sensors. *Nano Lett.* **2006**, *6*, 1747–1751.

98. Lim, J.; Simanek, E. E. Triazine Dendrimers as Drug Delivery Systems: From Synthesis to Therapy. *Adv. Drug Delivery Rev.* **2012**, *64*, 826–835.

99. Flebbe, T.; Hentschke, R.; Hädicke, E.; Schade, C. Modeling of Polyvinylpyrrolidone and Polyvinylimidazole in Aqueous Solution. *Macromol. Theory Simul.* **1998**, *7*, 567–577.

100. Lee, H.; Venable, R. M.; MacKerell, A. D., Jr; Pastor, R. W. Molecular Dynamics Studies of Polyethylene Oxide and Polyethylene Glycol: Hydrodynamic Radius and Shape Anisotropy. *Biophys. J.* **2008**, *95*, 1590–1599.

101. Vanommeslaeghe, K.; Hatcher, E.; Acharya, C.; Kundu, S.; Zhong, S.; Shim, J.; Darian, E.; Guvench, O.; Lopes, P.; Vorobyov, I.; et al. CHARMM General Force Field: A Force Field for Drug-like Molecules Compatible with the CHARMM All-atom Additive Biological Force Fields. *J. Comput. Chem.* **2010**, *31*, 671–690.

102. Royal Society of Chemistry. *ChemSpider*; 2015; http://www.chemspider.com (accessed Jan 2015).

103. O'Boyle, N. M.; Banck, M.; James, C. A.; Morley, C.; Vandermeersch, T.; Hutchison, G. R. Open Babel: An Open Chemical Toolbox. *J. Cheminf.* **2011**, *3*, 33.

104. Vanommeslaeghe, K.; MacKerell, A. D., Jr Automation of the CHARMM General Force Field (CGenFF) I: Bond Perception and Atom Typing. *J. Chem. Inf. Model.* **2012**, *52*, 3144–3154.

105. Vanommeslaeghe, K.; Raman, E. P.; MacKerell, A. D., Jr Automation of the CHARMM General Force Field (CGenFF) II: Assignment of Bonded Parameters and Partial Atomic Charges. *J. Chem. Inf. Model.* **2012**, *52*, 3155–3168.

106. Aksimentiev, A.; Brunner, R.; Cohen, J.; Comer, J.; Cruz-Chu, E.; Hardy, D.; Rajan, A.; Shih, A.; Sigalov, G.; Yin, Y.; et al. *Nanostructure Design: Methods and Protocols*; Methods in Molecular Biology; Humana Press, 2008; Vol. 474; pp 181−234.

107. Comer, J.; Wells, D. B.; Aksimentiev, A. *DNA Nanotechnology*; Humana Press, 2011; Vol. 749; Chapter 22, pp 317−358.

108. Humphrey, W.; Dalke, A.; Schulten, K. VMD - Visual Molecular Dynamics. *J. Mol. Graphics* **1996**, *14*, 33–38.

109. Phillips, J. C.; Braun, R.; Wang, W.; Gumbart, J.; Tajkhorshid, E.; Villa, E.; Chipot, C.; Skeel, R. D.; Kale, L.; Schulten, K. Scalable Molecular Dynamics with NAMD. *J. Comput. Chem.* **2005**, *26*, 1781–1802.

110. Towns, J.; Cockerill, T.; Dahan, M.; Foster, I.; Gaither, K.; Grimshaw, A.; Hazlewood, V.; Lathrop, S.; Lifka, D.; Peterson, G. D.; et al. XSEDE: Accelerating Scientific Discovery. *Comput. Sci. Eng.* **2014**, *16*, 62–74.

111. Feller, S. E.; Zhang, Y. H.; Pastor, R. W.; Brooks, B. R. Constant Pressure Molecular Dynamics Simulations − The Langevin Piston Method. *J. Chem. Phys.* **1995**, *103*, 4613–4621.

112. Darden, T. A.; York, D. M.; Pedersen, L. G. Particle Mesh Ewald: An $N \log N$ Method for Ewald Sums in Large Systems. *J. Chem. Phys.* **1993**, *98*, 10089–10092.

113. Miyamoto, S.; Kollman, P. A. SETTLE: An Analytical Version of the SHAKE and RATTLE Algorithm for Rigid Water Molecules. *J. Comput. Chem.* **1992**, *13*, 952–962.

114. Andersen, H. Rattle: A "velocity" Version of the Shake Algorithm for Molecular Dynamics Calculations. *J. Comput. Phys.* **1983**, *52*, 24–34.

115. Tuckerman, M. E.; Berne, B. J.; Martyna, G. J. Reversible Multiple Time Scale Molecular Dynamics. *J. Chem. Phys.* **1992**, *97*, 1990–2001.

116. Fiorin, G.; Klein, M. L.; Hénin, J. Using Collective Variables to Drive Molecular Dynamics Simulations. *Mol. Phys.* **2013**, *111*, 3345–3362.

117. Pohorille, A.; Jarzynski, C.; Chipot, C. Good Practices in Free-energy Calculations. *J. Phys. Chem. B* **2010**, *114*, 10235–10253.

118. Comer, J.; Phillips, J. C.; Schulten, K.; Chipot, C. Multiple-Walker Strategies for Free-Energy Calculations in NAMD: Shared Adaptive Biasing Force and Walker Selection Rules. *J. Chem. Theory Comput.* **2014**, *10*, 5276–5285.